Chemical Engineering Journal 520 (2025) 166083

Contents lists available at ScienceDirect

Chemical Engineering Journal

journal homepage: www.elsevier.com/locate/cej

Genetically engineered bacteria outer membrane vesicles coated small-molecule organic dye facilitates cDC1s-mediated antitumor immune cascade response for NIR-II tumor photoimmunotheranostics

Yuhao Chen [a,b,1], Xiaorui Geng [a,b,1], Ganipisetti Hanumantha Rao [c], Wei-Chih Wei [c], Addanki Venkateswararao [c], Tzu-Ming Liu [d,*], Ken-Tsung Wong [c,e,**], Yun Li [f], Pu Chun Ke [g], Zhen Yuan [a,b,***]

[a] Cancer Center, Faculty of Health Sciences, University of Macau, Taipa, Macau
[b] Centre for Cognitive and Brain Sciences, University of Macau, Taipa, Macau
[c] Department of Chemistry, National Taiwan University, Taipei 10617, Taiwan, Republic of China
[d] Institute of Translational Medicine, Faculty of Health Sciences, Ministry of Education Frontiers Science Center for Precision Oncology, University of Macau, Macau
[e] Institue of Atomic and Molecular Sciences, Academia Sinica, Taipei 10617, Taiwan, Republic of China
[f] Guangdong Yunzhao Medical Technology Co., LTD, Guangzhou 510641, China
[g] Drug Delivery, Disposition and Dynamics, Monash Institute of Pharmaceutical Sciences, Monash University, 381 Royal Parade, Parkville, VIC 3052, Australia

ARTICLE INFO

Keywords:
Engineered bacteria
OMV
NIR-II optical imaging
Immunotherapy
CD47

ABSTRACT

Although photothermal therapy (PTT) is a promising strategy for cancer treatment, the immunosuppressive tumor microenvironment promotes tumor progression and metastasis, limiting its effectiveness. To enhance adaptive antitumor immunity and improve post-PTT immunotherapy, genetically engineered bacteria outer membrane vesicles (OMVs)-modified small-molecule organic dye was constructed to serve as a nanophotosensitizer for NIR-II fluorescence/photoacoustic imaging-guided photo-immunotherapy. The developed nanophotosensitizer generated toxic hyperthermia under laser irradiation, promoting tumor antigen release. Meanwhile, the CD47nb-OMVs repolarized tumor-associated macrophages by blocking CD47-SIRRPα axis, relieving immunosuppressive tumor microenvironment. In addition, the present theranostic nanoplatform initiated tumor-resident type I conventional dendritic cells (cDC1s)-mediated antigen cross-presentation cascade, enhancing the downstream anti-tumor $CD8^+$ T cell response. Furthermore, *in vivo* tests by using triple-negative breast cancer mouse model demonstrated that the novel NIR-II nanophotosensitizer effectively transformed the immunologically cold tumor microenvironment into a hot one, significantly improve survival rates, and inhibit distant metastases.

1. Introduction

Triple-Negative Breast Cancer (TNBC) is a lethal female cancer with high metastasis and recurrence rate [1,2]. Meanwhile, photothermal therapy (PTT) as an emerging ablation therapy, can selectively destroy tumors without damaging the surrounding normal tissues, demonstrating its efficacy in the treatment of localized solid tumors [1]. Besides, PTT generates heat to induce cell apoptosis, resulting in strong immunogenic cell death (ICD) and antigen release [2,3]. However, the downside of PPT is that breast cancers treated with localized PTT might still develop recurrence or distal metastases due to the predominantly immunosuppressive tumor microenvironment (TME) such as inadequate immune cell infiltration, impaired immune cell function, and accumulation of immunosuppressive molecules [4–6]. In particular, the cold TME might promote immune evasion and tumor metastasis [7]. Therefore, immune reactivation is essential to improve the efficacy of antitumor therapy after PTT.

In addition, antigen presentation is a crucial process in the antitumor

* Corresponding author.
** Correspondence to: K.-T. Wong, Department of Chemistry, National Taiwan University, Taipei 10617, Taiwan, Republic of China.
*** Correspondence to: Z. Yuan, Cancer Center, Faculty of Health Sciences, University of Macau, Taipa, Macau.
E-mail addresses: tmliu@um.edu.mo (T.-M. Liu), kenwong@ntu.edu.tw (K.-T. Wong), zhenyuan@um.edu.mo (Z. Yuan).
[1] represents equal contribution to this work

https://doi.org/10.1016/j.cej.2025.166083
Received 6 May 2025; Received in revised form 19 June 2025; Accepted 15 July 2025
Available online 16 July 2025
1385-8947/

immune response. In particular, antigen cross-presentation by tumor-resident type I conventional dendritic cells (cDC1s) from major histocompatibility complex class I (MHC-I) to $CD8^+$ T cells exhibits the ability to boost anti-tumor response [8,9]. However, cDC1s dysfunction can lead to immunosuppressive responses for various solid tumors, including breast cancer [10]. In contrast, activating the antigen presentation cascade of cDC1s is a promising strategy to enhance the antitumor immunity of $CD8^+$ T cells. In particular, the activation of endogenous $CD8^+$ T cells is a complex multistep immune cascade, involving intratumor antigen uptake, activation, and migration to tumor-draining lymph nodes (TdLNs) [11,12]. During activation, cDC1 maturation is prevented by immunosuppressive molecules in the TME, such as TGF-β and IL-10 secreted by M2-phenotype tumor-associated macrophages (TAMs) [13–15]. Therefore, successfully reversing cDC1s dysfunction requires not only the presence of sufficient tumor-specific antigens but also the removal of immunosuppressive molecules within the TME.

More importantly, while PTT can induce ICD in tumor cells, its ability to remodel the TME is limited, making it challenging to activate tumor-resident cDC1s. In contrast, bacterial outer membrane vesicles (OMVs), which function similarly to bacteria, have demonstrated the potential for targeted tumor treatment. More interestingly, optimized OMVs prepared by genetically engineered bacteria, hold great promise for improved efficiency of cancer immunotherapy [16–18]. For example, functional OMVs-coated nanoplatform loaded with photosensitizers can improve drug delivery efficiency and concurrently remodel the immunosuppressive environment of solid tumors [19,20].

Furthermore, organic small molecules with near infrared (NIR) absorption and fluorescence properties are attractive sensitizers for various phototherapy applications [21,22]. More specifically, the donor-π-bridge-acceptor (D-π-A) architecture entails the advantage of NIR absorption, in which strong intramolecular charge transfer character renders the D-π-A-configured molecule to possess a high extinction coefficient, ensuring more effective light interaction. The optical properties of D-π-A-configured molecule can be feasibly modulated by the strategic selection of the D, π-bridge and A building blocks. To acquire optical absorption with wavelength higher than 700 nm, both the electronic properties of D and A and their aromatic/quinoidal characters need to be optimized. For example, the D-π-A-type molecule BT3, incorporating aromatic constituents with a high quinoidal character and a strong electron-acceptor (dicyanovinylene), demonstrated to have optical absorption of 802 nm with superior phototherapy efficeincy [23]. In addition, D-π-A-type molecules incorporating 1,3-indandione and its dicyanomethylene derivatives as the A moieties, which generate a pronounced ICT effect, have also been constructed for tumor phototherapy [24,25]. Typically, the D-π-A-type molecules are designed to have the D-π blocks linked to the exocyclic C═C bond at C2 position of the 1,3-indanedione-derived A groups for extending the π-conjugation [26,27]. In addition to 1,3-indanedione, indenone can also serve as a good A group. In particular, the derivatization of indenone to dicyanomethyleneindene (DCMI) which not only can induce strong ICT character to reduce the optical energy gap for efficient NIR absorption/emission, but also the increased structure stability of the desired emitter stemming from the endocyclic C═C bond linkage between D-π block and DCMI, impeding the propensity of possible nucleophilic attack onto the conjugated backbone. These figures make DCMI an intriguing new A structure for NIR active molecules.

In this study, a new molecular skeleton incorporating DCMI as a π-conjugated acceptor was constructed, which was linked to three different triarylamine donors for tuning the absorption. In particular, the one embedded with a high quinoidal π-bridge (BThDCMI) was used for the present work, exhibiting the absorption λ_{max} of 783 nm. To the best of our knowledge, this is the first study that used D-π-A-configured molecule with DCMI as A group for the development of NIR-II fluorescent organic small molecules for phototheranostics. To enhance the tumor photoimmunotheranostics, we developed a novel nanoplatform (OBDlp) for targeted PTT and subsequent cDC1s-mediated antigen cross-presentation. For the constructed OBDlp, BThDCMI was firstly loaded into liposome (BDlp), and then genetically engineered bacteria OMVs (CD47nb-OMVs) were coated onto BDlp to produce OBDlp. Guided by dual-modal fluorescence/photoacoustic imaging, the OBDlp serves as the photosensitizer for targeted PTT, further inducing ICD and M1-phenotype macrophage polarization, activating the robust cDC1s/$CD8^+$ T cells anti-tumor immune cascade response, and inhibiting breast tumor development (Fig. 1). Therefore, the combination of the immune cascade response and PTT presents a novel strategy for TNBC treatment, highlighting its significant potential in advancing tumor immunotherapy.

2. Results

2.1. Preparation and characterization of OBDlp

Here we report a new molecular skeleton incorporating DCMI as a π-conjugated acceptor, which is linked to three different triarylamine donors for tuning the absorption (Fig. 2a). The syntheses and characterization of the tailor-made DCMI-based molecules are provided in the Supporting Information (Fig. S1–9). The absorption and emission spectra recorded for the construct are depicted in Fig. 2b-d. In particular, BThDCMI, embedded with a high quinoidal π-bridge exhibiting the absorption λ_{max} of 783 nm and the emission of 930 nm (Fig. 2d), was selected for PTT and NIR-II optical imaging.

To enhance the immunotherapeutic function of bacterial outer membrane vesicles (OMVs), we fused the CD47 nanobody gene and the outer membrane ClyA coding region using a flexible linker for plasmid pBAD_CD47nb-ClyA construction (Fig. 2e). The recombinant plasmid vector was transformed into attenuated *E. coli* MG1655 to generate OMVs expressing the CD47 nanoantibody (CD47nb-OMVs). Successful expression of CD47nb-ClyA protein in engineered bacteria and OMVs induced by different concentrations of L-arabinose was confirmed by SDS-PAGE (Fig. 2e) and western blotting (Fig. S10). To test the function of CD47nb on OMVs, 4T1 breast cancer cells were incubated with OMVs and CD47nb-OMVs, respectively. The binding rate of FITC-labelled CD47 antibody was determined by flow cytometry. Gradually decreased CD47 antibody binding was detected when 4T1 cells were incubated with CD47nb-OMVs, indicating that CD47nb on the surface of OMVs can competitively bind to CD47 on 4T1 cells (Fig. 2f). The ability of CD47nb-OMVs to enhance macrophage phagocytosis was assessed. 4T1-GFP cells were pre-treated with PBS, OMVs or CD47nb-OMVs and then co-incubated with macrophages while the ratio of GFP^+ to $F4/80^+$ cells were detected by using flow cytometry. We discovered that CD47nb-OMVs treatment group exhibited significantly enhanced phagocytosis by macrophages as compared to the PBS and OMVs groups. OMVs alone also enhanced phagocytosis, indicating that CD47nb-OMVs activated macrophages through combination of CD47 blockade and bacterial stimulatory adjuvants (Fig. 2g). In addition, CD47nb-OMVs displayed a significant stimulatory effect on macrophages polarization, resulting in increased CD80 expression and decreased CD206 expression (Fig. 2h-i).

Subsequently, we encapsulated BThDCMI into the liposome (BDlp) using the thin film hydration method to enhance aqueous solubility of the drug. The mixture of CD47nb-OMVs and BDlp was repeatedly extruded by mechanical forces using an extruder, resulting in the coating of CD47nb-OMVs on BDlp (OBDlp). Transmission electron microscopy (TEM) images revealed that both BDlp and OBDlp were spherical-like structures (Fig. 2j). Dynamic light scattering (DLS) analysis illustrated that the hydrodynamic particle sizes of OMV, BDlp and OBDlp were ~ 12 nm, ~ 91 nm, and ~ 122 nm, respectively (Fig. 2k). The zeta potential values of OMVs, BDlp and OBDlp were − 8.58 ± 0.65 mV, −3.48 ± 0.65 mV, and − 6.28 ± 0.76 mV, respectively (Fig. S11). The surface potential of OBDlp was lower than BDlp, indicating successful modification of CD47nb-OMVs. The UV absorption spectra showed that BDlp and OBDlp entailed characteristic peaks similarly to

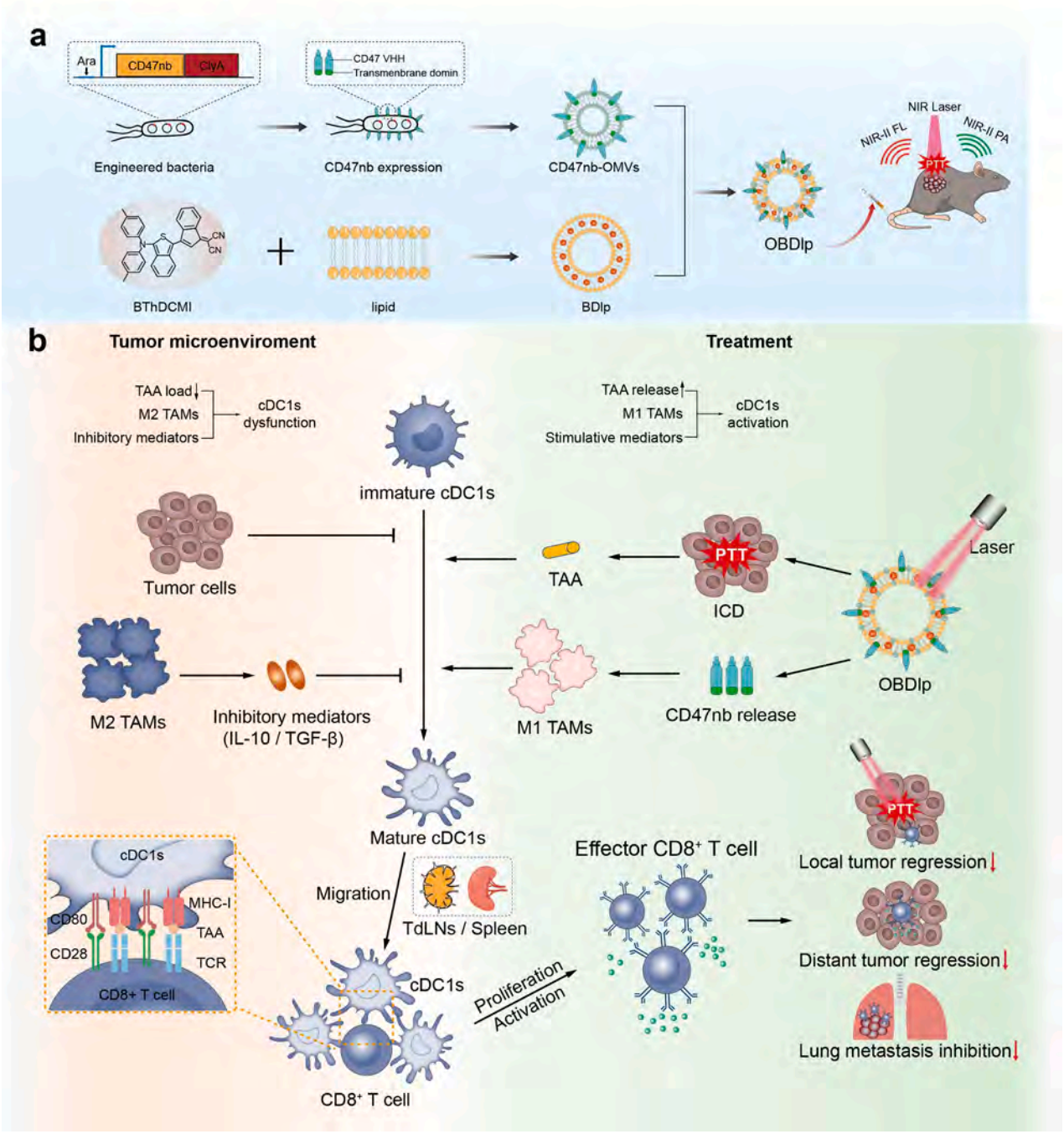

Fig. 1. Schematic of as-prepared OBDlp and the OBDlp-mediated PPT for cDC1s/$CD8^{+}$T cells anti-tumor immune cascade response. Upon being delivered to tumor sites, OBDlp can induce tumor cells ICD and release DAMPs under laser irradiation. CD47nb facilities the repolarization of M2-phenotype macrophages to M1-phenotype macrophages, which alleviate the obstruction of immunosuppressive microenvironment to cDC1s maturation. Thus, cDC1s are successfully activated in the remodeled "hot" tumor microenvironment, triggering downstream $CD8^{+}$ T cells anti-tumor immune cascade response against distant invasion and lung metastases.

that of BThDCMI, with peaks at ~ 783 nm (Fig. 2l). Fluorescence spectra showed that OBDlp had a distinct characteristic peak ~ 930 nm and was extended to the NIR II window, suggesting that OBDlp has the potential as a contrast agent for enhanced NIR II optical imaging (Fig. 2m). The encapsulation rate of OBDlp was 64.9 %, and that of BDlp was 62.3 % (Fig. S12). We further investigated the *in vitro* NIR II fluorescence imaging signals of different concentrations of BDlp or OBDlp solutions. The NIR II fluorescence imaging intensity of BDlp or OBDlp solutions was enhanced with increased concentrations from 1 to 80 μg/mL (Fig. 2n). In addition, OBDlp showed good stability. Under PBS conditions, no significant fluctuations in particle size or polydispersity index (PDI) of OBDlp were observed within 5 days (Fig. S13).

2.2. *In vitro photothermal therapy*

To explore the potential anti-tumor mechanisms, we first evaluated the 4T1 cellular uptake of BDlp or OBDlp. Flow cytometry showed that the uptake of OBDlp was significantly greater than that of BDlp at 4 h post-treatment (Fig. S14). In addition, encapsulating the small molecule dye into liposomes may contribute to improved photothermal stability.

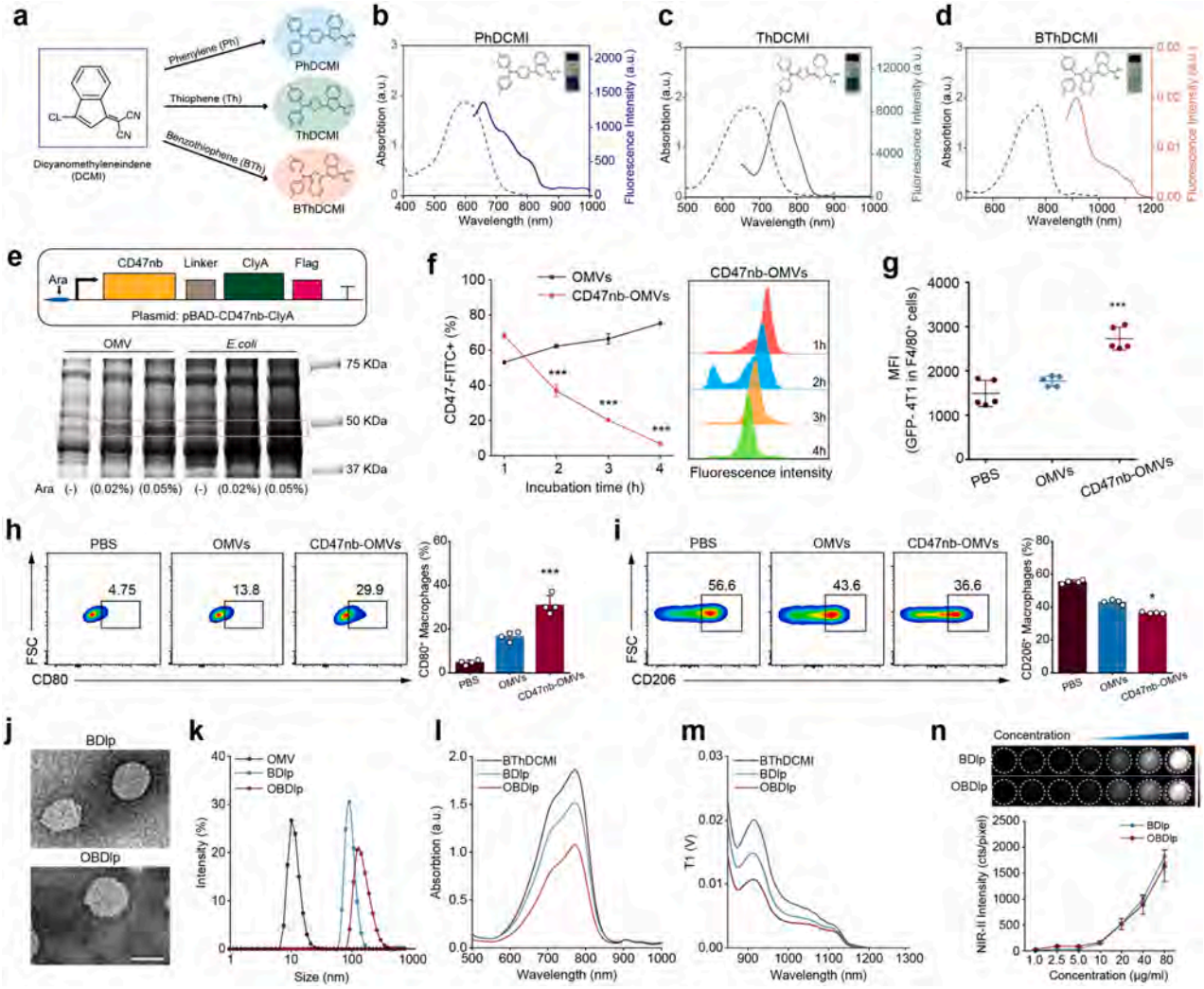

Fig. 2. Preparation and characterization of OBDlp. (a) Structures of PhDCMI, ThDCMI and BThDCMI. Absorption and photoluminescent spectra of (b) PhDCMI, (c) ThDCMI, and (d) BThDCMI. (e) Plasmid of CD47nb-OMVs and SDS-PAGE of engineered *E.coli* MG1655 and OMVs. (f) CD47 antibody binding rate of 4T1 cells after different treatments. (g) *In vitro* phagocytosis of 4T1 cells by macrophages after different treatments. (h) CD80 expression of macrophages received different treatments. (i) CD206 expression of macrophages with different treatments. (j) TEM images of BDlp and OBDlp. Scale bar = 100 nm. (k) Size distributions of OMVs, BDlp and OBDlp. (l) Absorption spectra of BThDCMI, BDlp and OBDlp. (m) Fluorescence spectra of BThDCMI, BDlp and OBDlp. (n) NIR II fluorescence intensities of BDlp and OBDlp solutions.

We found that the temperature decay of OBDlp was less than 7 % through four consecutive laser irradiation cycles. In marked contrast, free Indocyanine green (ICG) exhibited substantial temperature decay (~24.27 %) (Fig. 3a). This indicates that OBDlp can be used for PTT with good photothermal stability. Furthermore, we investigated the tumor cytotoxicity of OBDlp-mediated PTT. Live/dead staining showed that OBDlp with laser treatment effectively inhibited 4T1 cell viability. Treatment with OBDlp or BDlp alone elicited no significant cytotoxicity (Fig. 3b). Cell counting kit-8 (CCK-8) analysis showed that the viability of 4T1 cells was reduced to 37.94 ± 4.77 % after OBDlp with laser treatment (Fig. 3c). These results suggest that OBDlp possesses the potential for a novel photosensitizer to effectively kill breast tumor cells *via* PTT.

To inspect whether OBDlp-mediated PTT was able to trigger ICD and further contribute to dendritic cells (DCs) maturation, calreticulin (CRT), high mobility group protein 1 (HMGB1) and ATP as damage-associated molecular patterns (DAMPs) indicator were analyzed. We discovered that OBDlp with laser treatment induced more pronounced CRT exposure in 4T1 cells (Fig. 3d). ELISA assay showed the intracellular HGMB1 concentration and intracellular ATP levels in OBDlp with laser group were significantly lower than those in the control group (Fig. 3e-f). These findings illustrated that OBDlp-mediated PTT was able to effectively trigger ICD and enhance immunogenicity in 4T1 cells. Subsequently, we inspected whether PTT-induced ICD could promote DCs maturation. Following co-incubation of OBDlp with laser-treated tumor cell culture medium, the proportion of $CD80^{+}CD86^{+}$ DCs were analyzed by flow cytometry. In comparison with other treatment groups, OBDlp with laser-treated group exhibited a significantly elevated level of DCs maturation (Fig. 3g, j), correlated with enhanced TNF-α secretion and suppressed IL-10 production (Fig. 3h, i).

2.3. *In vivo* NIR II fluorescence/photoacoustic tumor imaging

The incorporation of OMVs intends to enhance the hypoxic-targeting ability of nanoparticles. To assess the tumor targeting efficacy of OBDlp, OBDlp or BDlp were administered intravenously to 4T1 tumor-bearing mice, and *in vivo* fluorescence imaging was performed at the indicated time points. OBDlp exhibited higher accumulation at the tumor area at 48 h post-injection compared to that of BDlp (Fig. 4a, e). Tumors and organs were collected at 48 h post-injection for *ex vivo* imaging. Mouse tumors of the OBDlp group showed significantly greater signals than the BDlp group, suggesting that the modification of OMVs significantly

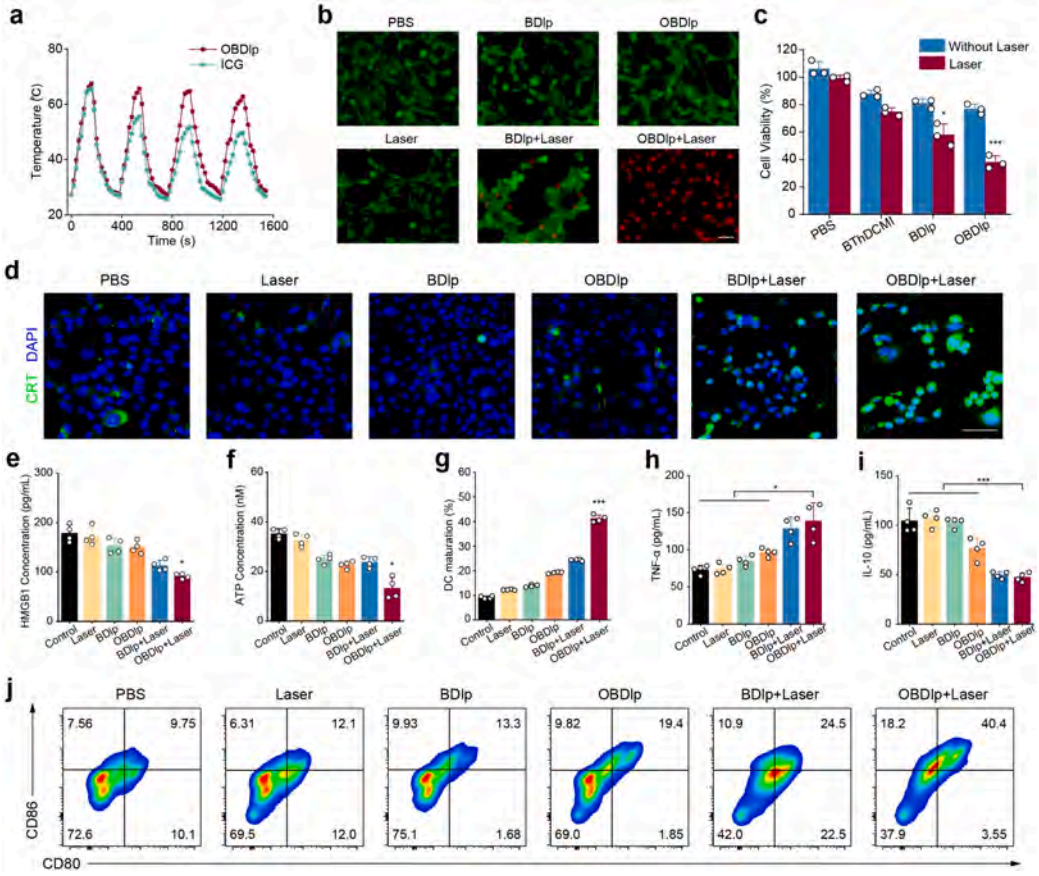

Fig. 3. *In vitro* photothermal therapy and DCs maturation. (a) Temperature change of OBDlp or free ICG solution irradiated with laser (808 nm, 1 W/cm^2). (b) Live/dead staining of 4T1 cells received with different treatment. Scale bar = 25 μm. (c) Cell viability of 4T1 cells treated with PBS, BThDCMI, BDlp or OBDlp with or without laser irradiation. (d) Immunofluorescence staining against CRT on 4T1 cells received different treatments. Scale bar = 25 μm. (e) HMGB1 level of 4T1 cells. (f) ATP level of 4T1 cells. (g) Maturation of DCs stimulated with medium derived from tumor cells received different treatments. (h) TNF-α level of DCs. (i) IL-10 level of DCs. (j) Flow cytometry blot of $CD80^+CD86^+$ DCs.

enhanced the tumors targeting of the nanophotosensitizer (Fig. 4b, f). Regarding the tumor targeting ability of OBDlp, it may be due to the modification of OMVs, which confers hypoxic targeting capability to the nanoparticles and enables tumor cells in hypoxic regions of tumors to actively uptake and retain the nanoparticles. Optical imaging in the NIR II windows entails a deeper imaging depth and greater signal-to-noise ratio compared to normal optical imaging. We further evaluated the ability of OBDlp to enhance *in vivo* fluorescence imaging in the NIR II windows. Fluorescence imaging (excitation: 808 nm, emission: 1075 nm) of tumor-bearing mice also showed that OBDlp accumulated in tumor tissues within 48 h, exhibiting significantly strong fluorescence signals (Fig. 4c, g). Fluorescence imaging in NIR-II can be used to precise monitor the photosensitizer distribution in the tumor tissue. *Ex vivo* imaging revealed that OBDlp accumulated more in the tumor tissue than BDlp (Fig. 4d). In particular, accumulation of OBDlp in the liver was significantly reduced compared with that of BDlp, indicating that OBDlp may ease the adverse effects caused by excessive accumulation of photosensitizers in organs (Fig. 4h).

Owing to its exceptional photothermal conversion efficiency, OBDlp demonstrates a significant potential for enhancing NIR-II photoacoustic imaging. *In vivo* photoacoustic imaging showed that the morphology and density of tumor microvessels were more clearly observable after OBDlp injection (Fig. 4i). Quantitative analysis further indicated that OBDlp group maintained significantly higher tumor signal intensity compared to the BDlp group at the 48 h post-injection (Fig. 4j). These observations suggested the feasibility of OBDlp to serve as a NIR-II fluorescence imaging/photoacoustic imaging contrast agent for tumor targeting imaging.

2.4. *In vivo anti-tumor therapy*

Encouraged by the *in vitro* tumor cells treatment results, we explored the therapeutic effect of OBDlp combined with laser in 4T1 tumor-bearing mice. 4T1 cells were transplanted subcutaneously in Balb/c mice to establish the breast tumor-bearing mouse model. Once the tumor volume reached approximately 100 mm^3, the mice were randomly divided into the following six groups for treatment: Control group and Laser group received PBS intravenously injection; BDlp group and BDlp+Laser group received BDlp intravenously injection; OBDlp group and OBDlp+Laser group received OBDlp intravenously injection. Two days later, the mice tumors of the Laser, BDlp+Laser and OBDlp+Laser groups were irradiated with 808 nm laser (Fig. 5a). The change in local tumor temperature with laser irradiation was detected by infrared thermometer. We discovered that OBDlp with laser irritation (808 nm, 1 W/cm^2, 10 min) significantly elevated the temperature of tumor site as compared to the other treatment groups (Fig. S15). No tumor growth inhibition was found in the Laser group. Tumor growth treated with BDlp alone and OBDlp alone was also not significantly inhibited. In contrast, 4T1 tumor-bearing mice treated with BDlp with laser showed a slight tumor suppression effect, and the combination of OBDlp with laser treatment significantly improved the antitumor effect (Fig. 5b). On day 15 after treatment, the tumor weight of mice treated with OBDlp combined with laser therapy was 0.54 ± 0.15 g, and the tumor inhibition rate was 65.87 % compared to the Control group (Fig. 5c-e). Furthermore, OBDlp combined with laser led to a substantial prolongation of survival in 4T1 tumor-bearing mice (Fig. 5f). Moreover, the body weight of mice treated with OBDlp combined with laser did not

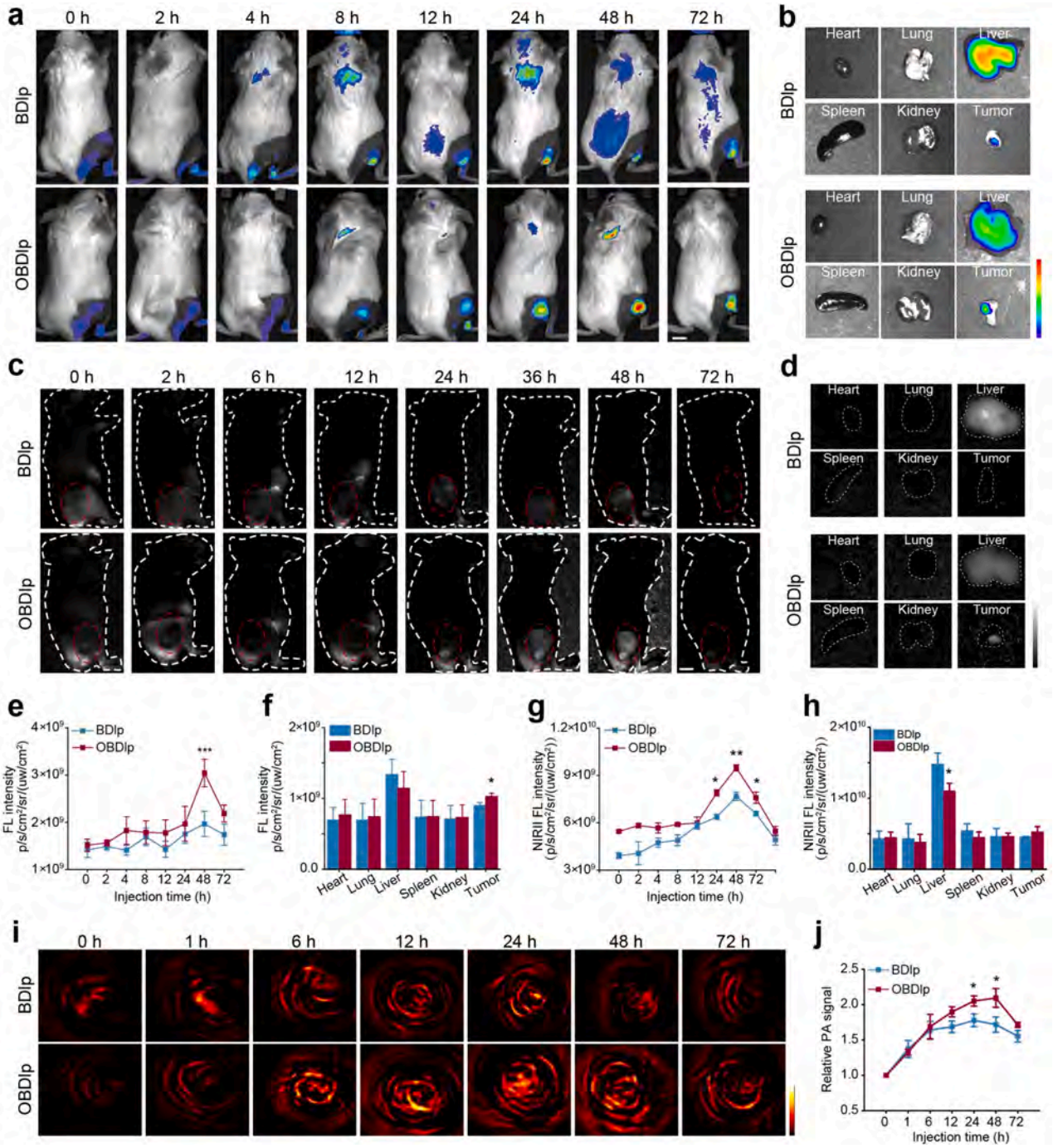

Fig. 4. *In vivo* NIR-II fluorescence/photoacoustic tumor imaging. (a) *In vivo* fluorescence imaging of tumor-bearing mice. Scale bar = 10 mm. (b) *Ex vivo* fluorescence imaging of organs and tumors. (c) NIR-II fluorescence imaging of tumor-bearing mice. Scale bar = 10 mm. (d) *Ex vivo* NIR-II fluorescence imaging of organs and tumors. (e) Quantitative analysis of fluorescence signal intensities of tumor-bearing mice. (f) Quantitative analysis of fluorescence signal intensity of *ex vivo* organs and tumors. (g) Quantitative analysis of NIR-II fluorescence signal intensities of tumor-bearing mice. (h) Quantitative analysis of NIR-II fluorescence signal intensity of *ex vivo* organs and tumors. (i) *In vivo* NIR-II photoacoustic imaging of tumor-bearing mice. (j) Quantitative analysis of photoacoustic imaging signal intensities of tumor-bearing mice.

change significantly during the treatment process (Fig. 5g). TUNEL staining further confirmed that OBDlp with laser treatment induced maximal 4T1 cell apoptosis, demonstrating the therapeutic effect of OBDlp combined laser with treatment for triple-negative breast tumors (Fig. 5h).

2.5. OBDlp-mediated PTT induced activation of cDC1s

We further investigated the therapeutic mechanism of OBDlp-mediated PTT to explore whether it achieved an effective anti-tumor immune response by enhancing the activation of tumor-resident cDC1s. We also established the 4T1 tumor-bearing mice model and adopted the previous experimental protocol. On day 7 after treatment, tumors, tumor-draining lymph nodes (TdLNs) and spleens were collected from each group of mice for immunological analysis.

First, we analyzed the polarization of macrophages within tumor tissues (Fig. S16). Flow cytometry revealed that OBDlp combined with laser treatment significantly increased the proportion of M1 phenotype

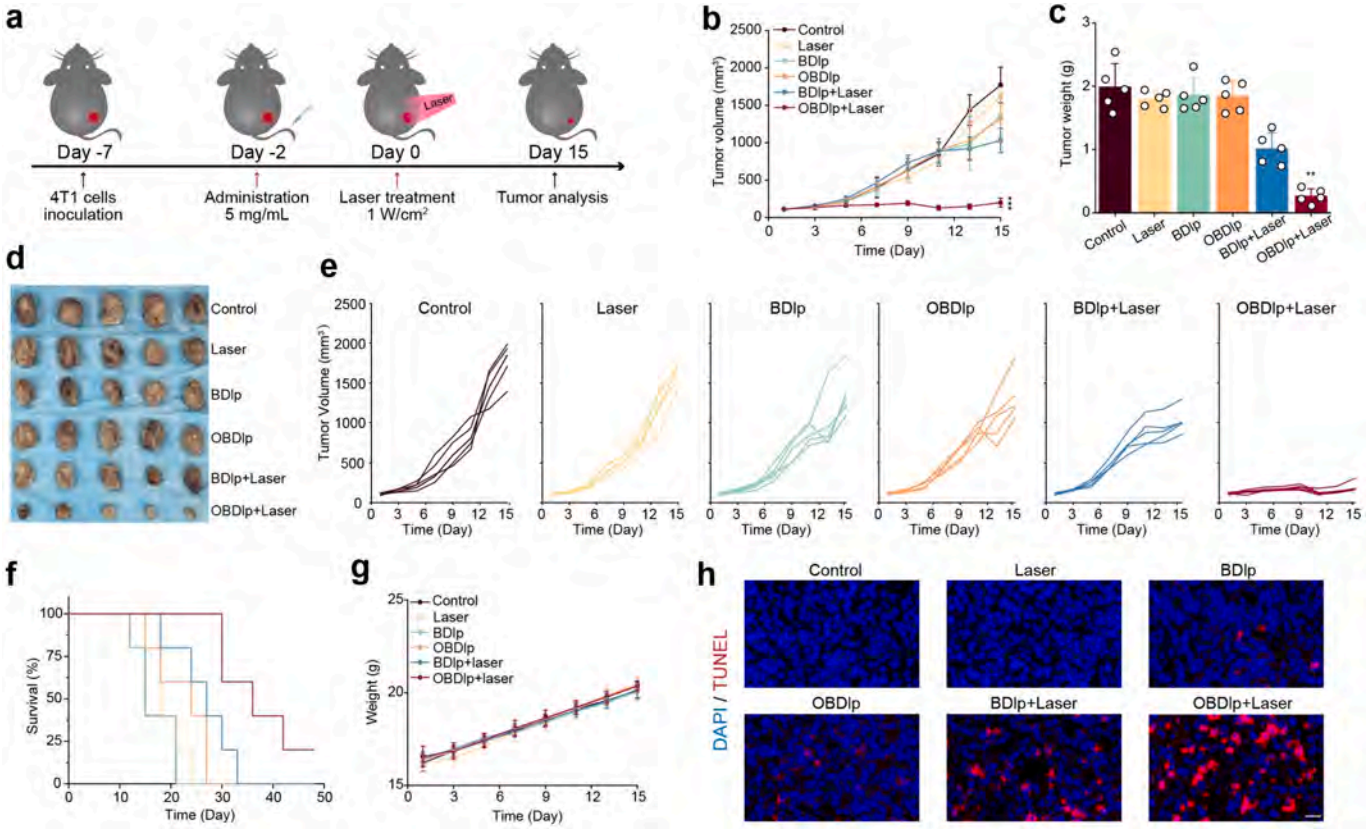

Fig. 5. *In vivo* anti-tumor therapy. (a) Schematic of the treatment procedure in 4T1 tumor-bearing mice. (b) Tumor volume change in treated mice. (c) Tumor weight of each group. (d) Photograph of harvested mice tumors. (e) Tumor volume changes in each group. (f) Survival time of treated mice. (g) Changes in body weight of mice during treatment. (h) TUNEL staining of tumors in different groups of mice. Scale Bar = 100 μm.

macrophages ($CD80^+F4/80^+CD11b^+$) in tumor tissues, resulting in a significantly greater M1/M2 macrophage ratio compared with other groups (Fig. 6a-b, Fig. S17a and Fig. S18a-c). Notably, OBDlp with laser treatment also promoted the polarization of the M1 phenotype of macrophages in spleen (Fig. 6a, c, Fig. S17b, Fig. S18d-e), which may be attributed to the blocking effect of CD47-SIRPα axis.

Repolarization of TAMs and PTT remodels the immunosuppressed tumor microenvironment and contributes to the activation of tumor-resident cDC1s. Subsequently, by analyzing the levels of cDC1s in tumor tissues, we observed that OBDlp combined with laser treatment significantly increased the proportion of cDC1s ($CD103^+CD11b^-CD11c^+$) (Fig. 6d, Fig. S19). The proportion of cDC1s increased from 4.81 % to 38.7 % in the laser combined OBDlp treatment group, as compared with the Control group (Fig. 6e). OBDlp with laser treatment also significantly increased the proportion of total DCs ($MHCII^+CD11c^+CD45^+$) within the tumor (Fig. S20a-b). The intratumoral cDC1s/cDC2s ratio was also significantly elevated after treatment (Fig. 6g). In particular, CD86 expression in the population of cDC1s was significantly increased after OBDlp with laser treatment, with CD86 levels nearly 2.0-fold higher than those in the Control group (Fig. 6h). These results suggested that OBDlp combined with laser treatment can induce the proliferation and maturation of tumor-resident cDC1s.

Tumor-resident cDC1s, stimulated by tumor-associated antigens, migrate to TdLNs to activate cytotoxicity $CD8^+$ T cells. Analysis of cDC1s in TdLNs showed that OBDlp combined with laser treatment also significantly increased the proportion of total DCs and cDC1s in TdLNs (Fig. 6d, Fig. S20c-e). The proportion of cDC1s in TdLNs after treatment with OBDlp combined with laser was 1.89-fold higher than that in the Control group, indicating that our treatment promoted the migration of tumor-resident cDC1s to TdLNs (Fig. 6f). Consistently, CD86 expression of cDC1s within TdLNs was significantly increased after OBDlp with laser treatment (Fig. 6i).

Collectively, these findings suggested that OBDlp combined with laser treatment enhanced the infiltration, maturation and migration of tumor-resident cDC1s *via* promoting ICD and M1 phenotype macrophage repolarization, thereby establishing the foundation for anti-tumor immunotherapy.

2.6. OBDlp-mediated PTT improved $CD8^+$ T cell immune response

Mature cDC1s bind to the T cell antigen receptor (TCR) on T cells *via* the antigenic peptide-MHC complex to activate cytotoxic $CD8^+$ T cells for enhanced anti-tumor immune response. Therefore, we further analyzed the T cells in TdLNs. As shown in Fig. 7a and Fig. S21, OBDlp combined with laser treatment resulted in a significant increase in the proportion of $CD8^+$ T cells within TdLNs. However, the proportion of $CD4^+$ T cells in TdLNs did not show significant changes. The proportion of proliferative $CD8^+$ T cells ($Ki67^+CD8^+CD3^+$) in TdLNs of mice treated with OBDlp combined laser was significantly increased, while the proportion of depleted $CD8^+$ T cells ($Tim3^+CD8^+CD3^+$) was significantly decreased (Fig. 7b). In addition, the proportion of functional $CD8^+$ T cells ($TNF\text{-}\alpha^+CD8^+CD3^+$) and functional $CD4^+$ T cells ($TNF\text{-}\alpha^+CD4^+CD3^+$) after OBDlp combined with laser treatment was 2.5-fold and 3.24-fold higher than that of the Control group (Fig. 7c-e), suggesting that improved cDC1s may contribute to the activation of $CD8^+$ T cells. Notably, the proportion of regulatory T (Treg) cells in the TdLNs of the OBDlp with laser group was significantly decreased compared with the other groups (Fig. S22a, c).

We then evaluated the tumor infiltrating T cells, which is crucial for anti-tumor immune response. Flow cytometry analysis of tumor tissue samples showed that the proportion of $CD4^+$ T cells and CD8+ T cells

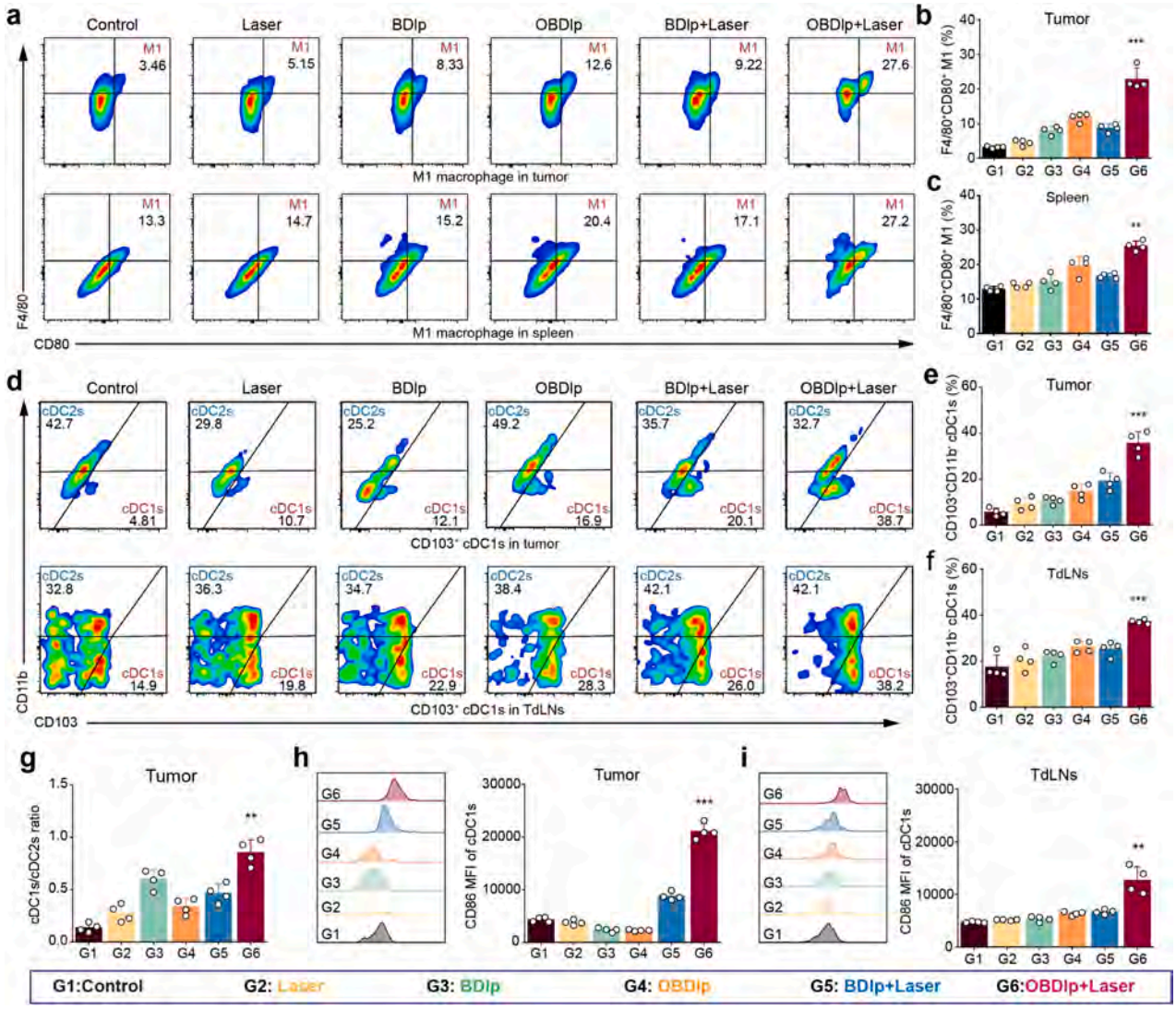

Fig. 6. OBDlp-mediated PTT improved M1 phenotype macrophages polarization and cDC1s maturation. (a) Flow cytometry plots of M1 phenotype macrophages in tumor and spleen. (b) Quantitative analysis of M1 phenotype macrophages in tumor. (c) Quantitative analysis of M1 phenotype macrophages in spleen. (d) Flow cytometry plots of cDC1s, cDC2s in tumors and TdLNs. (e) Quantitative analysis of cDC1s in tumors. (f) Quantitative analysis of cDC1s in TdLNs. (g) Quantitative analysis of the ratio of cDC1s/cDC2 in tumor. (h) Flow cytometry plots and quantitative analysis of CD86 in cDC1s in tumors. (i) Flow cytometry plots and quantitative analysis of CD86 in cDC1s in TdLNs.

within the tumor tissue was significantly higher in the OBDlp with laser treatment group (Fig. S23a). In particular, compared to the Control group, OBDlp with laser treatment significantly increased the proportion of proliferative $CD8^+$ T cells and functional $CD8^+$ T cells within tumors (Fig. 7d, f and Fig. S23b). After OBDlp combined with laser treatment, the proportion of depleted $CD8^+$ T cells and Treg cells in the tumor was significantly reduced, suggesting that T cell dysfunction was alleviated within the remodeled tumor immune microenvironment, which may be beneficial for PD-1/PD-L1 immune checkpoint inhibitor therapy (Fig. S22a-b, Fig. S23b). Immunofluorescence staining showed a significant increase in $CD8^+$ T cell and $CD4^+$ T cell intratumoral infiltration after OBDlp with laser treatment (Fig. 7g). These results indicate that OBDlp combined with laser treatment effectively activated tumor-infiltrating cytotoxic $CD8^+$ T cells.

The levels of pro-inflammatory cytokines IFN-γ, TNF-α, and IL-6 in the tumors of mice treated with OBDlp combined with laser treatment were significantly higher than those of the Control group (Fig. 7i-k). In addition, anti-inflammatory cytokine TGF-β was significantly reduced after treatment (Fig. 7l). Notably, a similar phenomenon was also observed in the peripheral blood, further indicating that adaptive immunity against the tumor was activated (Fig. S24).

Taken together, these results suggested that OBDlp combined with laser treatment enhanced anti-tumor immunotherapy by activating cDC1s-mediated antigen cross-presentation cascade through the following steps:(i) The CD47 nanobody carried by OBDlp induced polarization of M1 phenotype macrophages and remodels the immunosuppressive TME; (ii) OBDlp-mediated PTT enhanced tumor cell immunogenicity by triggering TAA release; (iii) ICD-released TAA and M1 phenotype macrophages synergistically activated cDC1s; (iv) Mature cDC1s and "hot" TEM further activated tumor infiltrating cytotoxic CD8+ T cells for antitumor immunity.

2.7. Inhibition of distant tumor invasion and lung metastasis

Since OBDlp combined with laser treatment effectively activates anti-tumor immunity, we next determined whether the immune response induced by this treatment strategy could inhibit distal tumor growth. A bilateral subcutaneous tumor-bearing mouse model was used to evaluate the therapeutic effect of OBDlp combined with laser treatment on distant tumors (Fig. 8a). Laser, BDlp, OBDlp and BDlp with laser

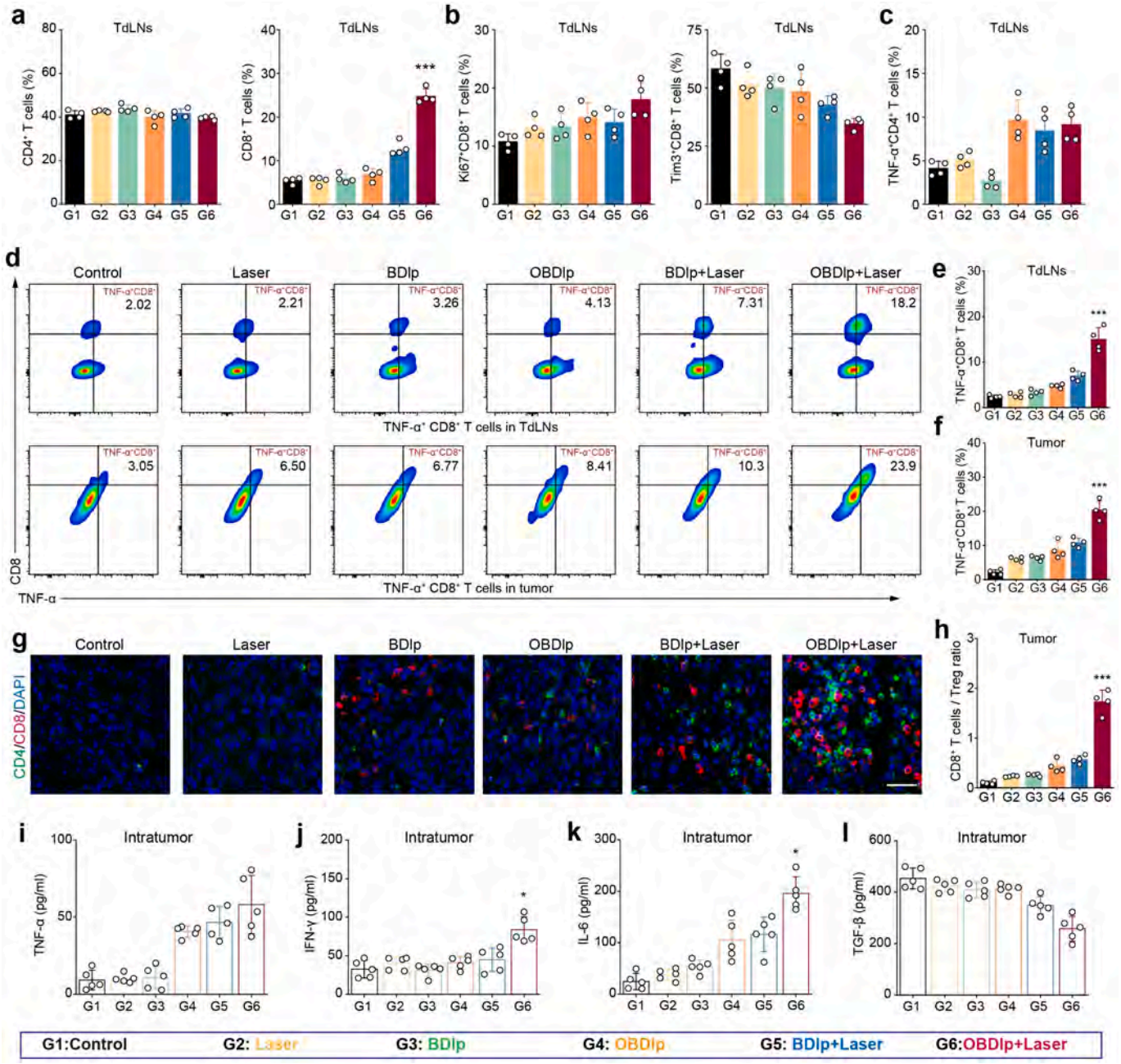

Fig. 7. OBDlp-mediated PTT induced proliferation and activation of T cells. (a) Quantitative analysis of $CD4^+$ T cells and $CD8^+$ T cells in TdLNs. (b) Quantitative analysis of proliferative $CD8^+$ T cells and exhausted $CD8^+$ T cells in TdLNs. (c) Quantitative analysis of functional $CD4^+$ T cells in TdLNs. (d) Flow cytometry plots of functional $CD8^+$ T cells in tumors and TdLNs. (e) Quantitative analysis of functional $CD8^+$ T cells in TdLNs. (f) Quantitative analysis of functional $CD8^+$ T cells in tumors. (g) $CD4^+/CD8^+$ immunofluorescence staining in tumors. Scale bar = 40 μm. (h) Quantitative analysis of $CD8^+$ T cell/Treg ratio in tumors. (i) TNF-α levels in tumors. (j) IFN-γ levels in tumors. (k) IL-6 levels in tumors. (l) TGF-β levels in tumors.

treatments had limited effects on distant tumors. In contrast, OBDlp with laser treatment significantly inhibited distant tumor growth (Fig. 8b-d). At day 15 after treatment, both primary and distant tumor weights in the OBDlp with laser-treated group were significantly lower than those in the other groups (Fig. 8e). Due to the inhibition of distant tumor, the survival time of mice in the OBDlp with laser-treated group was significantly prolonged than BDlp with laser-treated group (Fig. 8f). Notably, we found that OBDlp with laser treatment significantly increased DCs maturation and M1 phenotype macrophage polarization within the distant tumor, as evidenced by a rise in the proportion of $CD80^+CD86^+$ DCs and an increase in the proportion of $F4/80^+CD80^+$ macrophages (Fig. 8g-h, Fig. S25). Meanwhile, the activation of antigen-presenting cells led to a significant increase in $CD8^+$ T cell levels within the distant tumor, accompanied by enhanced proliferation and functionality of $CD8^+$ T cells (Fig. 8i and Fig. S26).

Next, we evaluated whether OBDlp with laser treatment could effectively inhibit the lung metastasis of breast tumor. As revealed by H&E staining of lung sections, the number of lung metastases and lung weight in the OBDlp with laser-treated group were significantly lower than those in the Control and OBDlp-treated groups (Fig. 8 l-m). These findings indicated that OBDlp, in combination with laser treatment, induced a systemic immune response by activating antigen-presenting cells in the spleens and TdLNs. In addition, the remodeling of the "hot" tumor microenvironment also prevented the migration and

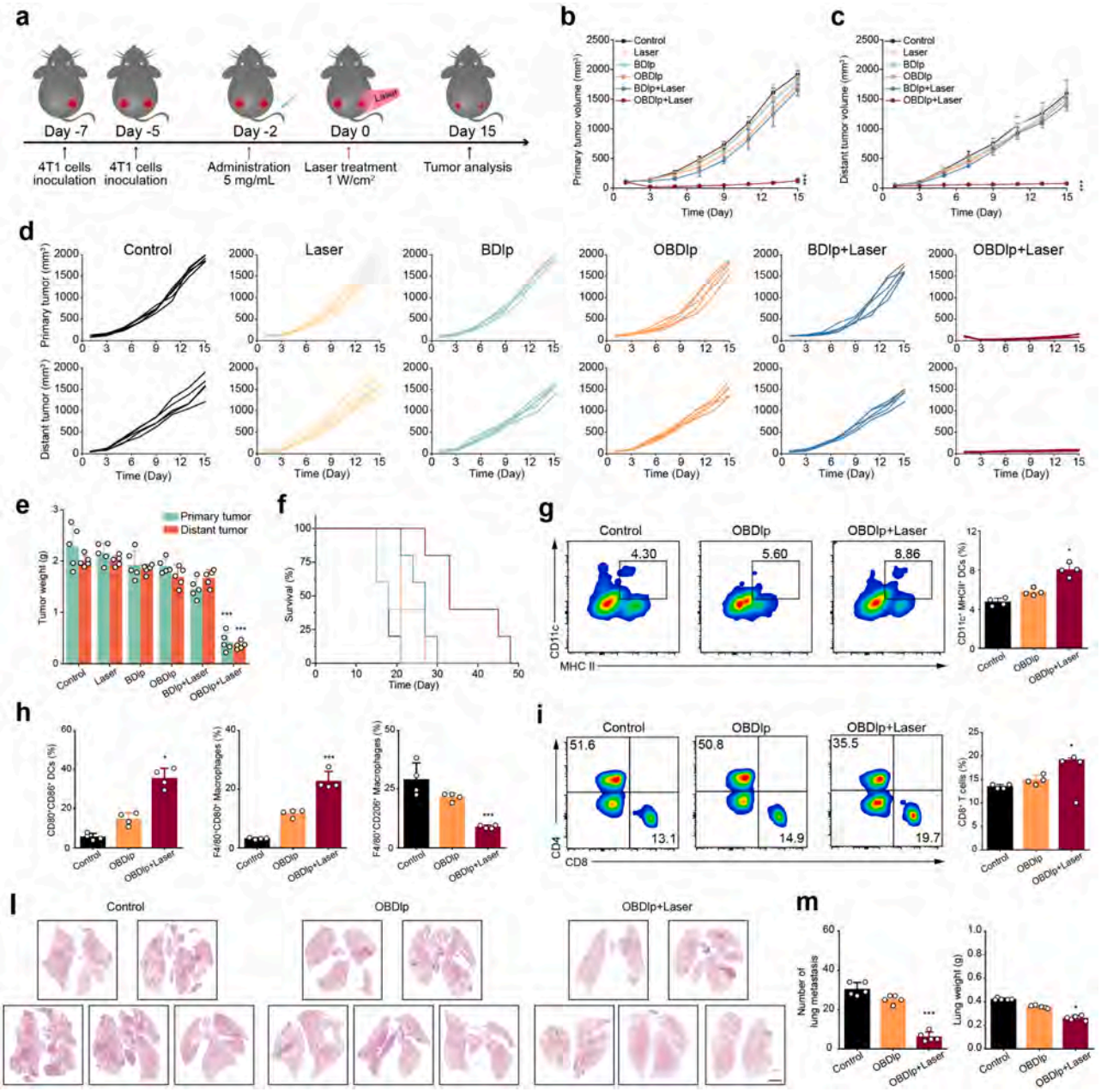

Fig. 8. Treatment of OBDlp-mediated PTT for distant tumor invasion and lung metastasis. (a) Schematic diagram of the treatment procedure in mice with bilateral tumors. (b) Primary tumor volume change in treated mice. (c) Distant tumor volume change in treated mice. (d) Primary tumor and distant tumor volume changes in each group. (e) Primary tumor and distant tumor weights. (f) Survival time of treated mice. (g) Flow cytometry plots and quantitative analysis of DCs in distant tumors. (h) Quantitative analysis of mature DCs, M1 phenotype macrophages, M2 phenotype macrophages in distant tumors. (i) Flow cytometry plots and quantitative analysis of $CD8^+$ T cells in distant tumors. (l) H&E staining sections of mice lungs from different groups. Scale bar = 2.5 mm. (m) Quantitative analysis of lung metastasis and lung weight of each group.

metastasis of tumor cells.

2.8. Evaluation of the role of cDC1s and $CD8^+$ T cells for distant tumors inhibition

The immunological analyses described above revealed that the anti-tumor immune response triggered by OBDlp combined with laser treatment was mainly dependent on cDC1s and $CD8^+$ T cells. Therefore, we performed the rescue experiments to evaluate the role of cDC1s and CD8+ T cells in immunotherapy against distant tumors (Fig. 9a). Migration of cDC1s was blocked by injection of anti-MHC-I antibody. $CD8^+$ T cells were also depleted by the corresponding antibody. In addition, OBDlp combined with laser treatment improved the tumor infiltrating $CD8^+$ T cell dysfunction, which might be beneficial for anti-PD-L1 antibody treatment. Therefore, the therapeutic efficiency of combination of anti-PD-L1 antibody and OBDlp with laser treatment was also tested. As shown in Fig.9a, bilateral tumor-bearing mice were randomly divided into six groups. Specifically, Control group received PBS injection. The other groups received combined OBDlp and laser treatment, along with injections of control antibody isotype IgG, anti-CD8 antibody, anti-MHC-I antibody and anti- PD-L1 antibody, respectively.

The results of tumor growth in mice showed that blockade of MHC-I or depletion of $CD8^+$ T cells significantly interfered with the antitumor effect of OBDlp combined with laser treatment. This suggested important contributions of cDC1s and $CD8^+$ T cells in the efficacy entailed by

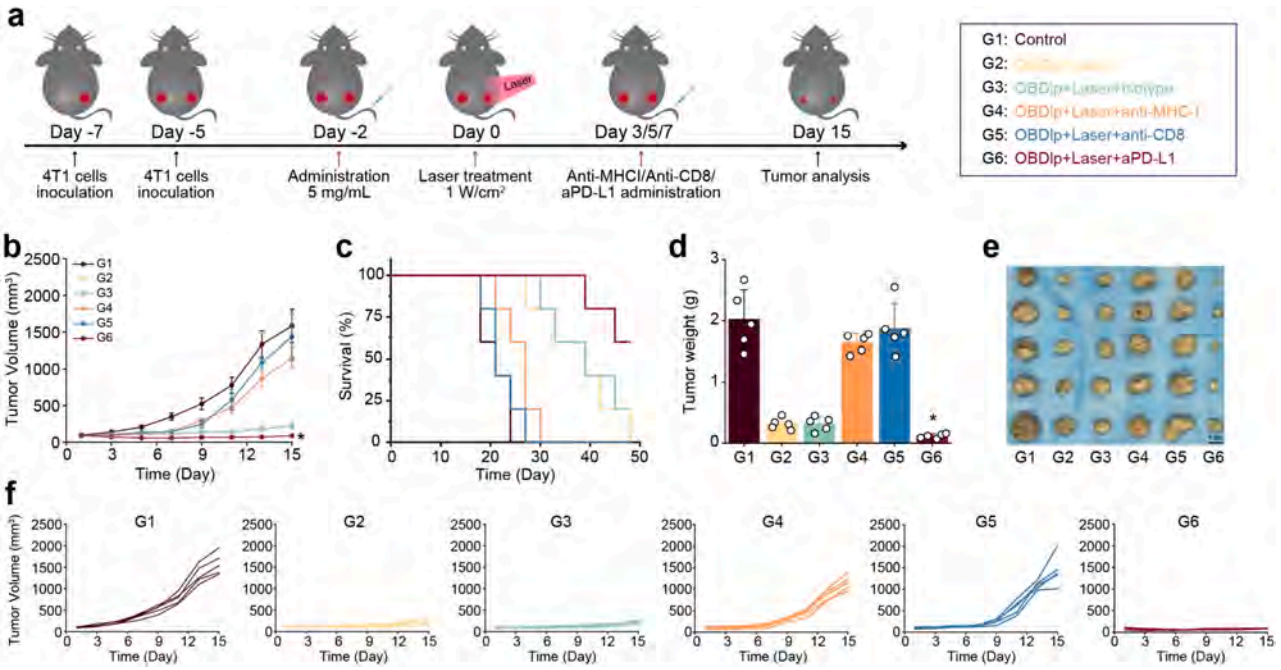

Fig. 9. Evaluation of the role of cDC1s and $CD8^+$ T cells for distant tumors inhibition. (a) Schematic of the treatment procedure of *in vivo* experiment. (b) Distant tumor volume change in treated mice. (c) Survival time of treated mice. (d) Distant tumor weight f treated mice. (e) Photographs of collected distant tumors. Scale bar = 1 cm. (f) Distant tumor volume changes of each group.

OBDlp combined with laser treatment. Notably, OBDlp with laser combined with anti-PD-L1 antibody treatment significantly inhibited the growth of distant tumors, and the tumor inhibition efficacy even exceeded that of the OBDlp with laser group (Fig. 9d-f). At 50 days after tumor inoculation, the survival rates of tumor-bearing mice treated OBDlp with laser combined with anti-PD-L1 antibody were above 60 % (Fig. 9c) indicating that co-administration of anti-PD-L1 antibody significantly improved the therapeutic efficacy of OBDlp combined with laser treatment. Furthermore, OBDlp combined with laser treatment did not cause significant changes in liver and kidney function indicators in mice and organs histopathology, demonstrating the biological safety of OBDlp (Fig. S27).

3. Conclusions

In conclusion, the preparation of OBDlp by introducing a tailor-made NIR active small molecule BThDCMI into genetically engineered OMVs provided a novel nanophotosensitizer that mediated tumor-targeted PTT *via* NIR-II FL/PA imaging for cDC1s-mediated antitumor immune cascade response. OBDlp combined with laser induced DAMPs release and improved tumor immunogenicity. Meanwhile, CD47 nanobody carried on the nanophotosensitizers induced M1 phenotype macrophage polarization by blocking the CD47-SIRPα signaling axis, remodeling the immunosuppressive TME. Furthermore, activated cDC1s induced proliferation and functionalization of endogenous $CD8^+$ T cells, laying a foundation for effective anti-tumor immunotherapy. Overall, NIR-II imaging-guided photo-immunotherapy effectively inhibited the growth and metastasis of triple-negative breast cancer *via* enhancing the activation of cDC1s.

4. Methods

4.1. Synthesis of small molecule organic dyes

Here we report a new molecular skeleton incorporating dicyanomethyleneindene (DCMI) as a π-conjugated acceptor, which is linked to three different triarylamine donors for tuning the absorption. The detailed synthetic route was shown in Supplementary Fig. 1. Among them, BThDCMI embedded with a high quinoidal π-bridge exhibited the absorption λ_{max} of 783 nm, which was selected for the phototherapy application. The reaction between the compound 1a and phosphoryl chloride in *N, N*-dimethylaniline yielded chlorobenzofulvene. Compound 2 was treated with [4-[bis-(4- methylphenyl)amino]phenyl] boronic acid (4) by using Suzuki-Miyaura coupling to give PhDCMI. Compound 2 was used to undergo Stille coupling with compound 8 and 10 to give ThDCMI and BThDCMI respectively. Compounds 2, 4, 8, and 10 were prepared according to reported procedures [23,28–30]. The NMR spectrum of PhDCMI, ThDCMI and BThDCMI was shown in Supplementary Fig. 2–9.

4.2. Synthesis of bacterial OMV expressing CD47nb

To produce CD47nb-OMV, a DNA fragment encoding a fusion protein of ClyA (bacterial outer membrane surface protein) and CD47nb (CD47nb-ClyA) was inserted into the expression plasmid pBAD. The DNA fragment encoding the CD47nb-ClyA fusion protein was synthesized by BGI Company and cloned into the pBAD plasmid using the one-step Gibson assembly method. The plasmid was then transformed into *E. coli* MG1655. The engineered bacteria were cultured in LB medium supplemented with chloramphenicol (25 μg/mL) in a shaker for 200 rpm at 37 °C. When the OD_{600} reached approximately 0.5, CD47nb-ClyA protein expression was induced by the addition of 0.05 % arabinose at 37 °C for 16 h. The bacterial suspension was then collected, the bacteria were removed by centrifugation through a 0.45 μm filter membrane, and OMV-CD47nb was collected by ultracentrifugation.

The capacity of CD47nb-OMV to enhance macrophage phagocytosis was assessed. RAW 264.7 macrophages were inoculated into 96-well plates with 5×10^4 cells per well. The 4T1-GFP cells were pre-treated with PBS, OMV or CD47nb-OMV for 2 h. Pre-treated 4T1 cells were co-incubated with macrophages in a 2:1 ratio at 37 °C for 4 h. After washing with PBS, flow cytometry was performed to investigate the ratio of GFP^+ cells to $F4/80^+$ cells to assess phagocytosis of tumor cells by macrophages.

4.3. Preparation and characterization of OBDlp

DPPC, DSPC, DOPC and cholesterol were dissolved in chloroform at a molar ratio of 5:3:1:1. BThDCMI (2 mg/mL) dissolved in tetrahydrofuran (THF) was added. The solution was blown into a lipid film using nitrogen gas and dried thoroughly under vacuum. After dissolving the lipid film in PBS and adding CD47nb-OMV membrane protein, the solution was squeezed in extruder with pore size of 100 nm to prepare OBDlp. Free BThDCMI was removed by dialysis.

4.4. Tumor cells uptake

4T1 cells were incubated overnight in 24-well plates with 5×10^4 cells per well. Fresh medium with BDlp or OBDlp was replaced to co-incubate with 4T1 cells for different times. Cell uptake of nanoparticles was observed by fluorescence microscopy with flow cytometry.

4.5. In vitro cytotoxicity assay

OBDlp or indocyanine green (ICG) solution (50 μg/ml) was added to 96-well plates. Temperature changes of the solution under 808 nm laser irradiation (1 W/cm^2) were observed by an infrared thermography camera. 4T1 cells were planted in 96-well plates with 10,000 cells per well. After 24 h, the medium was replaced with fresh medium containing BThDCMI, BDlp, or OBDlp respectively. The cells were exposed to 808 nm laser irradiation (1 W/cm^2, 10 min). Cell viability was then determined by a CCK8 assay and live/dead cell staining.

4.6. In vitro macrophage polarization

4T1 cells were planted in 24-well plates and cultured overnight at 37 °C. Following above different treatment, 4T1 cells were fixed by 4 % paraformaldehyde. The cells were treated with a blocking solution for 30 min and then stained by DAPI for 5 min. The cells were washed with PBS and incubated with anti-CRT antibody for 2 h. The FITC-labelled secondary antibody was added to the cell wells. Fluorescence microscopy was used to observe the CRT exposure in 4T1 cells.

4.7. In vivo NIR II fluorescence imaging and photoacoustic imaging of OBDlp

Female Balb/c mice were employed to establish subcutaneous tumor-bearing mice models. 4T1 cells (1×10^6 cells each mouse) were injected subcutaneously into the back of mice. Once the mouse tumors grown to approximately 200 mm^3, OBDlp or BDlp (5 mg/kg) was intravenously injected into the tumor-bearing mice ($n = 3$). *In vivo* NIR II fluorescence/photoacoustic imaging was conducted at different time points. The mice were euthanized 48 h after injection, and the organs and tumors were collected for *ex vivo* imaging. BDlp and OBDlp were injected intravenously to tumor-bearing mice, and NIR II fluorescence imaging (excitation: 808 nm, emission: 1075 nm) was performed at different time points. The imaging signals were quantitatively analyzed with IVIS and Image J software.

4.8. Immune cells detection

Tumor-bearing mice were randomly divided into six groups ($n = 4$), including the Control group, Laser group, BDlp group, OBDlp group, BDlp+laser group and OBDlp+laser group. Seven days after receiving the different treatments, the mice were euthanized and the tumors, spleens and tumor-draining lymph nodes (TdLNs) were collected. Tissues were minced and processed by collagenase digestion to obtain single cell suspensions. The single-cell suspensions were incubated with fluorescently labelled antibodies at 4 °C for 30 min. Then Flow cytometry was used to analysize various subtypes of DCs, Macrophages and T cells.

4.9. Cytokine detection

On the seventh day after the administration of the various treatments, the tumor-bearing mice were euthanized and their peripheral blood and tumors were collected. The levels of various cytokines in the peripheral blood and tumor tissues were then analyzed according to the instructions of cytokine ELISA kits.

4.10. Inhibition of distant invasion and lung metastasis of breast tumor

4T1 cells (1×10^6 cells per mouse) were injected subcutaneously into the right dorsal of Balb/c mice to establish primary tumors. 3 days later, 4T1 cells (1×10^6 cells per mouse) were injected subcutaneously into the other dorsal of the mice to establish distant tumor-bearing mouse model. The mice were treated when their primary tumor volume reached approximately 100 mm^3. Tumor-bearing mice were divided into 6 groups ($n = 5$): (i) control group, (ii) laser group, (iii) BDlp group, (iv) OBDlp group, (v) BDlp+laser group, and (vi) OBDlp+laser group. BDlp or OBDlp (5 mg/kg) was intravenously injected, and 48 h later, the mice tumors were exposed to laser irradiation (808 nm, 1 W/cm^2, 10 min). Mice were continuously monitored for bilateral tumor volume and body weight changes after treatment. Mice were sacrificed on day 15 after treatment and bilateral tumors were harvested to measure tumor weight. Mouse lungs were collected to calculate the number of lung metastases.

4.11. Evaluation of the effect of CD8 and MHC-I blockade on distant tumors

4T1 cells (1×10^6 cells per mouse) were injected subcutaneously into the right dorsal of Balb/c mice to establish primary tumors. Two days later, 4T1 cells (1×10^6 cells per mouse) were injected subcutaneously into the other dorsal of the mice to establish a distant tumor-bearing mouse model. The mice were treated when their primary tumor volume reached approximately 100 mm^3. Tumor-bearing mice were divided into 5 groups (n = 5): (i) Control group, (ii) OBDlp+laser, (iii) OBDlp+laser+Isotype, (iv) OBDlp+laser+anti-MHC-I, (v) OBDlp+laser+anti-CD8 and (vi) OBDlp+laser+aPD-L1. The OBDlp (5 mg/kg) was intravenously injected, and 48 h later, the mice primary tumors were exposed to laser irradiation (808 nm, 1 W/cm^2, 10 min). Anti-CD8 antibody, anti-MHC-I antibody, isotype antibody and aPD-L1 were injected intraperitoneally at day 3, 5 and 7. Mice were continuously monitored for distant tumor volume and body weight changes after treatment. Mice were sacrificed on day 15 after treatment and distant tumors were harvested to measure tumor weight. Mouse lungs were collected to calculate the number of lung metastases.

CRediT authorship contribution statement

Yuhao Chen: Writing – original draft, Methodology, Data curation. **Xiaorui Geng:** Writing – review & editing, Methodology. **Ganipisetti Hanumantha Rao:** Methodology. **Wei-Chih Wei:** Methodology. **Addanki Venkateswararao:** Methodology. **Tzu-Ming Liu:** Methodology. **Ken-Tsung Wong:** Writing – review & editing, Methodology. **Yun Li:** Methodology. **Pu Chun Ke:** Writing – review & editing. **Zhen Yuan:** Writing – review & editing, Resources, Project administration, Conceptualization.

Declaration of competing interest

The authors declare that they have no known competing financial interests or personal relationships that could have appeared to influence the work reported in this paper.

Acknowledgements

This work is supported by the University of Macau (MYRGGRG2023-00038-FHS, MYRG2022-00054-FHS, MYRG-CRG2022-00009-FHS, and MYRG-GRG2023-00053-FHS-UMDF), Macao Science and Technology Development Fund (FDCT 0020/2019/AMJ, FDCT 0048/2021/AGJ, FDCT 0003/2023/RIC, and FDCT 0013/2023/RIC), and Higher Education Fund of Macao SAR Government Natural Science Foundation of Guangdong Province (EF017/FHS-YZ/2021/GDST), and National Science and Technology Council (NSTC-110-2113-M-002-008-MY3) Taiwan.

Appendix A. Supplementary data

Supplementary data to this article can be found online at https://doi.org/10.1016/j.cej.2025.166083.

Data availability

Data will be made available on request.

References

[1] J. Chen, T.X. Chen, Q.L. Fang, C.S. Pan, O.U. Akakuru, W.Z. Ren, J. Lin, A.Z. Sheng, X.H. Ma, A.G. Wu, Gd2O3/b-TiO2 composite nanoprobes with ultra-high photoconversion efficiency for MR image-guided NIR-II photothermal therapy, Exploration 2 (6) (2022), https://doi.org/10.1002/exp.20220014.
[2] M. Overchuk, R.A. Weersink, B.C. Wilson, G. Zheng, Photodynamic and Photothermal therapies: synergy opportunities for nanomedicine, ACS Nano 17 (9) (2023) 7979–8003, https://doi.org/10.1021/acsnano.3c00891.
[3] L. Tang, Q.Q. Xiao, Y. Yin, Y.J. Mei, J. Li, L. Xu, H.B. Gao, W. Wang, An enzyme-responsive and NIR-triggered lipid-polymer hybrid nanoplatform for synergistic photothermal/chemo cancer therapy, Biomater. Sci. 10 (9) (2022) 2370–2383, https://doi.org/10.1039/d2bm00216g.
[4] J.A. Joyce, D.T. Fearon, T cell exclusion, immune privilege, and the tumor microenvironment, Science 348 (6230) (2015) 74–80, https://doi.org/10.1126/science.aaa6204.
[5] K. Nakamura, M.J. Smyth, Myeloid immunosuppression and immune checkpoints in the tumor microenvironment, Cell. Mol. Immunol. 17 (1) (2020) 1–12, https://doi.org/10.1038/s41423-019-0306-1.
[6] L. Tang, H.N. Liu, Y. Yin, T. Pan, C. Fu, Y.Q. Cao, Y.J. Mei, Q.Q. Xiao, Z.W. Yan, Y. Yao, et al., Micro/nano system-mediated local treatment in conjunction with immune checkpoint inhibitor against advanced-stage malignant melanoma, Chem. Eng. J. (2024) 497, https://doi.org/10.1016/j.cej.2024.154499.
[7] F. Bayerl, P. Meiser, S. Donakonda, A. Hirschberger, S.B. Lacher, A.M. Pedde, C. D. Hermann, A. Elewaut, M. Knolle, L. Ramsauer, et al., Tumor-derived prostaglandin E2 programs cDC1 dysfunction to impair intratumoral orchestration of anti-cancer T cell responses, Immunity 56 (6) (2023) 1341–1358, https://doi.org/10.1016/j.immuni.2023.05.011.
[8] J.P. Böttcher, C.R.E. Sousa, The role of type 1 conventional dendritic cells in cancer immunity, Trends Cancer 4 (11) (2018) 784–792, https://doi.org/10.1016/j.trecan.2018.09.001.
[9] L.X. Huang, Y. Rong, X. Tang, K.Z. Yi, P. Qi, J.X. Hou, W.H. Liu, Y. He, X. Gao, C. H. Yuan, et al., Engineered exosomes as an in situ DC-primed vaccine to boost antitumor immunity in breast cancer, Mol. Cancer 21 (1) (2022), https://doi.org/10.1186/s12943-022-01515-x.
[10] T.L. Murphy, K.M. Murphy, Dendritic cells in cancer immunology, Cell. Mol. Immunol. 19 (1) (2022) 3–13, https://doi.org/10.1038/s41423-021-00741-5.
[11] C. Chen, Z.H. Wang, Y. Ding, Y.R. Qin, Tumor microenvironment-mediated immune evasion in hepatocellular carcinoma, Front. Immunol. 14 (2023), https://doi.org/10.3389/fimmu.2023.1133308.
[12] D.J. Theisen, J.T. Davidson, C.G. Briseño, M. Gargaro, E.J. Lauron, Q.L. Wang, P. Desai, V. Durai, P. Bagadia, J.R. Brickner, et al., WDFY4 is required for cross-presentation in response to viral and tumor antigens, Science 362 (6415) (2018) 694–699, https://doi.org/10.1126/science.aat5030.
[13] C. Luri-Rey, G. Gomis, J. Glez-Vaz, A. Manzanal, A.M. Riaño, M.E.R. Ruiz, A. Teijeira, I. Melero, Cytotoxicity as a form of immunogenic cell death leading to efficient tumor antigen cross-priming, Immunol. Rev. 321 (1) (2024) 143–151, https://doi.org/10.1111/imr.13281.
[14] C.S. Guo, Z.Y. You, H. Shi, Y. Sun, X.R. Du, G. Palacios, C. Guy, S.J. Yuan, N. M. Chapman, S.A. Lim, et al., SLC38A2 and glutamine signalling in cDC1s dictate anti-tumour immunity, Nature 620 (7972) (2023) 200–208, https://doi.org/10.1038/s41586-023-06299-8.
[15] G. Ghislat, A.S. Cheema, E. Baudoin, C. Verthuy, P.J. Ballester, K. Crozat, N. Attaf, C. Dong, P. Milpied, B. Malissen, et al., NF-κB-dependent IRF1 activation programs cDC1 dendritic cells to drive antitumor immunity, Sci. Immunol. 6 (61) (2021), https://doi.org/10.1126/sciimmunol.abg3570.
[16] J.M. Pan, X.L. Li, B.F. Shao, F.N. Xu, X.H. Huang, X. Guo, S.B. Zhou, Self-blockade of PD-L1 with bacteria-derived outer-membrane vesicle for enhanced cancer immunotherapy, Adv. Mater. 34 (7) (2022), https://doi.org/10.1002/adma.202106307.
[17] J.M. Pan, Z.H. Wang, X.H. Huang, J. Xue, S.L. Zhang, X. Guo, S.B. Zhou, Bacteria-derived outer-membrane vesicles hitchhike neutrophils to enhance ischemic stroke therapy, Adv. Mater. 35 (38) (2023), https://doi.org/10.1002/adma.202301779.
[18] R.J.R. Kelwick, A.J. Webb, P.S. Freemont, Opportunities for engineering outer membrane vesicles using synthetic biology approaches, Extracell. Vesicles Circ. Nucleic Acids 4 (2) (2023) 255–261, https://doi.org/10.20517/evcna.2023.21.
[19] C. Fu, L. Tang, Y.Q. Cao, Y. Yin, H.N. Liu, J.W. Feng, J.F. Gao, J. Li, W. Wang, Bacterial outer membrane vesicles-clothed nanoparticles delivered by live macrophages for potentiating antitumor photoimmunotherapy, Chem. Eng. J. 499 (2024), https://doi.org/10.1016/j.cej.2024.156420.
[20] Q.S. Lin, Y.C. Wang, L.L. Wang, Z.J. Fan, Engineered macrophage-derived cellular vesicles for NIR-II fluorescence imaging-guided precise cancer photo-immunotherapy, Colloids Surfaces B-Biointerfaces (2024) 235, https://doi.org/10.1016/j.colsurfb.2024.113770.
[21] Q. Xin, H.Z. Ma, H. Wang, X.D. Zhang, Tracking tumor heterogeneity and progression with near-infrared II fluorophores, Exploration 3 (2) (2023), https://doi.org/10.1002/exp.20220011.
[22] A.P. Nikam, P.D. Meshram, A.V. Vanjari, S.V. Mundada, Comparative study of spray-drying and freeze-drying techniques for increasing Fenofibrate's solubility and dissolution rate, BIO Integr. 5 (1) (2024) 1–11, https://doi.org/10.15212/bioi-2024-0010.
[23] Y.P. Wan, G.H. Lu, W.C. Wei, Y.H. Huang, S.L. Li, J.X. Chen, X. Cui, Y.F. Xiao, X. Z. Li, Y.H. Liu, et al., Stable organic photosensitizer nanoparticles with absorption peak beyond 800 nanometers and high reactive oxygen species yield for multimodality phototheranostics, ACS Nano 14 (8) (2020) 9917–9928, https://doi.org/10.1021/acsnano.0c02767.
[24] Z.J. Zhang, W.H. Xu, M.M. Kang, H.F. Wen, H. Guo, P.F. Zhang, L. Xi, K. Li, L. Wang, D. Wang, et al., An all-round athlete on the track of Phototheranostics: subtly regulating the balance between radiative and nonradiative decays for multimodal imaging-guided synergistic therapy, Adv. Mater. (2020) 32 (36), https://doi.org/10.1002/adma.202003210.
[25] X.L. Xu, G.J. Deng, Z.H. Sun, Y. Luo, J.K. Liu, X.H. Yu, Y. Zhao, P. Gong, G.Z. Liu, P. F. Zhang, et al., A biomimetic aggregation-induced emission photosensitizer with antigen-presenting and hitchhiking function for lipid droplet targeted photodynamic immunotherapy, Adv. Mater. 33 (33) (2021), https://doi.org/10.1002/adma.202102322.
[26] H. Gu, W.J. Liu, S.J. Zhen, S.R. Long, W. Sun, J.F. Cao, X.Z. Zhao, J.J. Du, J.L. Fan, X.J. Peng, "Internal and external combined" nonradiative decay-based Nanoagents for photoacoustic image-guided highly efficient Photothermal therapy, ACS Appl. Mater. Interfaces 13 (39) (2021) 46353–46360, https://doi.org/10.1021/acsami.1c14020.
[27] B. Lu, Z.C. Zhang, D.N. Jin, X.L. Yuan, J. Wang, Y. Ding, Y. Wang, Y. Yao, A-DA'D-A fused-ring small molecule-based nanoparticles for combined photothermal and photodynamic therapy of cancer, Chem. Commun. 57 (90) (2021) 12020–12023, https://doi.org/10.1039/d1cc04629b.
[28] Y.T. Liao, Y.C. Hsiao, Y.C. Lo, C.C. Lin, P.S. Lin, S.H. Tung, K.T. Wong, C.L. Liu, Solution-processed Isoindigo- and Thienoisoindigo-based donor-acceptor-donor it-conjugated small molecules: synthesis, morphology, molecular packing, and field-effect transistor characterization, ACS Appl. Mater. Interfaces 14 (50) (2022) 55886–55897, https://doi.org/10.1021/acsami.2c18049.
[29] S.H. Chou, H.C. Chen, C.K. Wang, C.L. Chung, C.M. Hung, J.C. Hsu, K.T. Wong, Synthesis and characterization of new asymmetric thieno 3,4-b pyrazine-based D -π - a - a type small molecular donors with near-infrared absorption and their photovoltaic applications, Org. Electron. 68 (2019) 159–167, https://doi.org/10.1016/j.orgel.2019.02.013.
[30] D. Stan, I. Baciu, A. Nicolae, L. Neagu, F. Dumitrascu, M. Matache, Synthesis of new 1,3-indandione derivatives, Rev. Chim. 60 (3) (2009) 264–268.